Light-induced Weyl semiconductor-to-metal transition mediated by Peierls instability

Honglie Ning [1,2,*] Omar Mehio,[1,2,*] Chao Lian,[3,*] Xinwei Li,[1,2] Eli Zoghlin [4] Preston Zhou,[2] Bryan Cheng [2]
Stephen D. Wilson,[4] Bryan M. Wong [3] and David Hsieh [1,2,†]

[1]*Institute for Quantum Information and Matter, California Institute of Technology, Pasadena, California 91125, USA*
[2]*Department of Physics, California Institute of Technology, Pasadena, California 91125, USA*
[3]*Department of Chemical and Environmental Engineering, Materials Science and Engineering Program, and Department of Physics and
Astronomy, University of California, Riverside, California 92521, USA*
[4]*Materials Department, University of California, Santa Barbara, California 93106, USA*

Elemental tellurium is a strongly spin-orbit coupled Peierls-distorted semiconductor whose band structure features topologically protected Weyl nodes. Using time-dependent density functional theory calculations, we show that impulsive optical excitation can be used to transiently control the amplitude of the Peierls distortion, realizing a mechanism to switch tellurium between three states: Weyl semiconductor, Weyl metal, and non-Weyl metal. Further, we present experimental evidence of this inverse Peierls distortion using time-resolved optical second harmonic generation measurements. These results provide a pathway to multifunctional ultrafast Weyl devices and introduce Peierls systems as viable hosts of light-induced topological transitions.

I. INTRODUCTION

Weyl nodes are topologically stable crossing points between nondegenerate bands in a crystal, which impart unconventional properties, including ultrahigh charge mobility and chiral magnetotransport [1]. The possibility to create or annihilate Weyl nodes *in situ* using ultrashort light pulses has been broadly explored theoretically [2–7] and was recently demonstrated experimentally in Dirac and type-II Weyl semimetal materials via impulsively driven lattice symmetry changes [8–11]. However, efforts have so far focused on binary switching between semimetallic states with and without Weyl nodes.

In this paper, we first use density functional theory (DFT) calculations to show a three-state switch from a Weyl semiconductor to a Weyl metal to a non-Weyl metal in chiral Peierls-distorted tellurium crystals as a function of the chiral chain radius. By performing time-dependent DFT calculations, we then demonstrate that these states can be transiently stabilized via a light-induced inverse Peierls distortion. Predicted signatures of the inverse Peierls distortion are experimentally reproduced using time-resolved optical second harmonic generation.

The Peierls instability is a spontaneous symmetry-lowering lattice deformation that lifts the degeneracy of electronic states at the Fermi level in order to reduce the overall system energy [Fig. 1(a)]. Elemental tellurium (Te) is a prototypical Peierls-distorted system, which crystallizes in a noncentrosymmetric trigonal structure composed of chiral chains of

Te atoms oriented along the *c* axis, with space group $P3_121$ or $P3_221$ depending on the chain chirality [Fig. 1(c) depicts the $P3_121$ structure]. Each atom has two intrachain nearest neighbors (NNs) and four interchain next-nearest neighbors (NNNs). This structure can be regarded as arising from the Peierls distortion of an achiral centrosymmetric rhombohedral structure (space group $R\bar{3}m$) in which the NN and NNN distances are equal [Figs. 1(d) and 1(f)] [12]. The structural evolution is parameterized by the chain radius x, expressed in units of the lattice constant or interchain distance a, which is a displacement along the A_1 phonon coordinate. In the equilibrium phase $x_{eq} = 0.269$, and at the structural phase transition (SPT) into the rhombohedral phase $x_{SPT} = 0.333$, amounting to a difference of around 0.26 Å.

II. NUMERICAL SIMULATION RESULTS

To understand the evolution of the electronic structure with x, we performed fully relativistic DFT calculations [13]. In the equilibrium phase ($x_{eq} = 0.269$), we find that Te is a semiconductor with nondegenerate bands harboring Weyl nodes (WNs) below the Fermi level along the H-K line in the Brillouin zone [Fig. 1(g)], as well as Kramers WNs [14] at the time-reversal-invariant momenta Γ, M, and A. These results are consistent with previous reports [15–19] classifying Te as a Weyl semiconductor (WS). To study the evolution of band topology in detail, we focus on a characteristic WN pair (WN1 and WN1′) near the Fermi level along K-H-K. Since WNs arise from a two-band crossing, their locations in momentum space can be identified by mapping the energy gap between the two bands [Fig. 1(i)]. This can be corroborated by additionally mapping the z component of spin polarization for the upper band, which is expected to reach a maximum amplitude with opposite signs at WN1 and WN1′ [16,17].

---

*These authors contributed equally to this work.
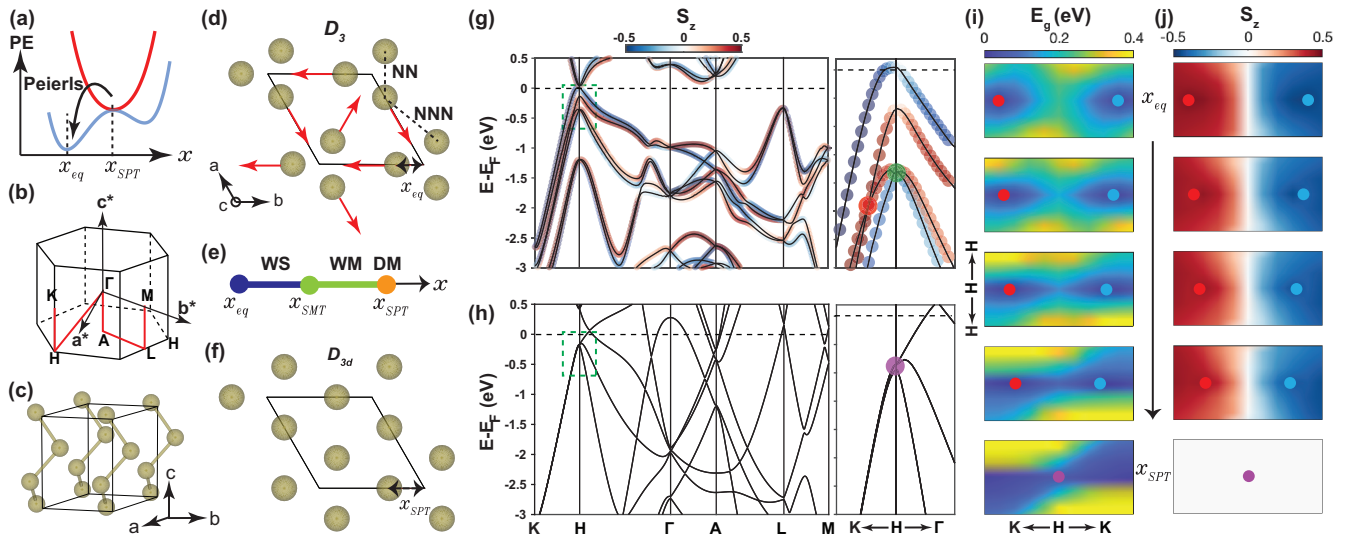†Author to whom correspondence should be addressed: dhsieh@caltech.edu

FIG. 1. Band evolution of Te across the Peierls transition. (a) Schematic evolution of the potential energy (PE) surface across a Peierls transition. (b) Brillouin zone and (c) unit cell of bulk Te. (d) Equilibrium structure of Te (D_3 point group). The black rhombus denotes the unit cell, and red arrows point along the A_1 phonon coordinate x. (e) Phase diagram as a function of x determined from DFT calculations (WS: Weyl semiconductor; WM: Weyl metal; DM: Dirac metal). (f) Peierls undistorted structure of Te (D_{3d} point group). (g) DFT calculated band structure of Te for the equilibrium and (h) Peierls undistorted structures. The color scale represents the spin polarization along z. Zooms on the window spanning 0.05 to -0.7 eV (dashed rectangle) are displayed on the right. Red, green, and purple circles mark WN1, the Kramers-Weyl node at H, and the Dirac node, respectively. (i) Momentum space maps of the energy gap between the two bands forming WN1 (red circle) and WN1′ (blue circle) and (j) the z component of spin polarization for the upper band at select x values of 0.269, 0.290, 0.305, 0.319, and 0.333 (top to bottom). The horizontal and vertical ranges of each panel span $-0.1c^*$ to $0.1c^*$ and $-0.05b^*$ to $0.05b^*$ relative to H, respectively, where b^* and c^* are the reciprocal lattice vectors defined in (b).

Upon increasing x, Te first undergoes a semiconductor-to-metal transition (SMT) at $x_{SMT} \approx 0.283$ [Fig. 1(e)] due to the sinking of the conduction bands at A [13]. At this stage, WN1 and WN1′ remain well separated, thus realizing an intermediate Weyl metal (WM). As x further increases, WN1 and WN1′ approach each other, and the energy gap along H-K continues to shrink, with little change in the spin texture [Figs. 1(i) and 1(j)]. Finally, on reaching the rhombohedral phase ($x_{SPT} = 0.333$), band degeneracy is restored, and a merger of WN1 and WN1′ into a Dirac node accompanies a closing of the direct gap near H [Figs. 1(h)–1(j)], giving rise to a Dirac metal (DM). Tuning x therefore provides a mechanism for simultaneous WN, spin texture, and band gap control.

Previous DFT studies have shown that trigonal Te can be driven into topological Weyl semimetal, three-dimensional topological insulator, or WM phases by applying either hydrostatic pressure or shear or uniaxial strains to alter its structure [19–21]. However, no equilibrium pathway to directly invert the Peierls distortion by tuning x, through either thermal or mechanical deformation [22,23], is known to exist.

Impulsive excitation by an intense laser pulse offers a potential out-of-equilibrium pathway to induce an inverse Peierls transition. By optically depopulating states near the Fermi level, the energy increase due to the lattice distortion is no longer balanced by the energy decrease due to the lifting of band degeneracy. This causes a sudden change in the potential energy surface of the lattice, generating a restoring force that drives coherent atomic motion reversing the Peierls distortion. For underdamped motion, a totally symmetric $A_{1(g)}$ Raman active mode is expected to be coherently launched through this

displacive excitation mechanism [13,24] [Fig. 1(a)]. Light-induced inverse Peierls transitions are accessible in a variety of systems including A7-structured semimetals [25], VO$_2$ [26], and charge density wave materials [27–29]. However, this mechanism has so far not been explored for ultrafast control of band topology.

To study the possibility of a light-induced inverse Peierls distortion in Te, we carried out time-dependent (TD) DFT calculations [13] to simulate the real-time lattice dynamics following impulsive optical excitation. Our method provides a fully *ab initio* description of the electronic, phononic, and photonic degrees of freedom on equal footing. Using an advanced evolutionary algorithm, the velocity-gauge formalism, and symmetry-reduced momentum space sampling, we efficiently calculate the periodic Te system up to an unprecedented 3 ps, providing comprehensive information about not only the fast electronic response but also the long-time structural dynamics. The pump pulse is chosen to have a Gaussian profile of 100 fs width, a linear polarization with electric field perpendicular to the c axis, and a photon energy centered at 1 eV, which is above the 0.3 eV band gap of Te. Otherwise, there are no adjustable parameters. For all pump fluences sampled, we resolved atomic motion exclusively along the A_1 phonon coordinate. Specifically, pumping excites sinusoidal displacement oscillations in time t about a new value of x that is shifted higher than x_{eq} [Fig. 2(a)]. Since the lifetime of photocarriers deduced from our simulations well exceeds our sampled time window of several picoseconds [13], this new position (x_0) is metastable. With increasing fluence F, both the magnitude of the oscillations and x_0 increase. At sufficiently high fluence x_0 is able to reach x_{SPT}, signifying complete
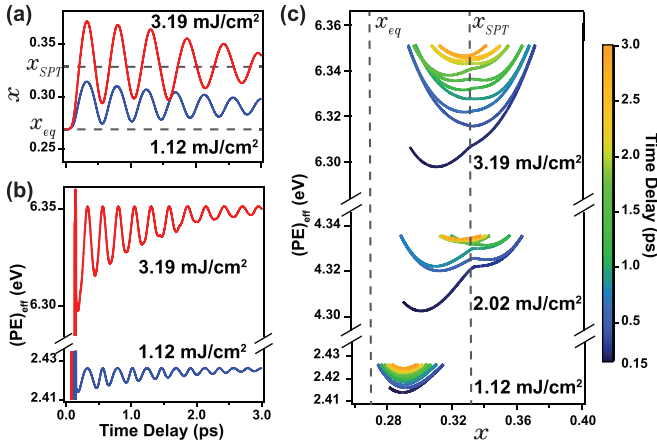
FIG. 2. Light-induced lattice and effective potential energy dynamics. TDDFT calculated temporal evolution of (a) x and (b) the effective potential energy (see text) following impulsive optical excitation at a fluence below (blue) and above (red) F_c. (c) Spatiotemporal trajectories of the effective potential energy at fluences below, near, and above F_c. Color scales with the time delay.

reversal of the Peierls distortion. An effective potential energy (PE$_{\text{eff}}$) can be determined by evaluating $E_{\text{total}}[x(t), t] - E_{\text{kin}}[x(t), t]$, which is the difference between the total energy (including both lattice and electronic degrees of freedom) and ionic kinetic energy [Fig. 2(b)]. To better visualize the dynamics of the inverse Peierls transition, we plot the spatiotemporal trajectory of PE$_{\text{eff}}$ for select fluences in Fig. 2(c). For a fixed fluence, we observe that PE$_{\text{eff}}$ generally increases with time because $E_{\text{total}}[x(t), t]$ is fixed, while $E_{\text{kin}}[x(t), t]$ is gradually damped out. But within each oscillation period there are local minima marking metastable x positions. In the low-fluence regime, the trajectories are parabolic and share a single minimum displaced slightly towards x_{SPT} from x_{eq}. As fluence increases, this minimum monotonically shifts to larger x and, near a critical value $F_c \approx 2$ mJ/cm² (0.03 V/Å peak field), the trajectories become flattened and highly nonparabolic. Above F_c, parabolic trajectories are restored about a new minimum fixed at x_{SPT}. The fluence dependence of the curvature and local minima of PE$_{\text{eff}}$ are signatures of a dynamical phase transition across F_c that can be quantitatively tested experimentally.

Our TDDFT simulations are consistent with several previously reported experiments. Time-resolved pump-probe x-ray diffraction measurements on Te showed that the lattice undergoes transient deformation predominantly along the A_1 coordinate [30], characterized by periodic oscillations about a position positively offset from x_{eq}. However, low fluences were used for this experiment, which induced changes in x only of the order of 0.01. Time-resolved optical reflectivity measurements demonstrated displacive excitation of coherent A_1 phonon oscillations, which undergo redshifting and chirping with increasing fluence [31–33], as well as an anomalous blueshift at higher fluence possibly due to overshooting a high-symmetry point, although no explicit claim of an inverse Peierls distortion was made [34]. Transient broadband optical spectroscopy measurements on Te thin films revealed slow photocarrier recombination times ranging from tens to

hundreds of picoseconds, possibly bottlenecked by weak intervalley scattering [35,36], giving rise to a metastable excited state. Finally, evidence of a semiconductor-to-metal transition [37] was revealed by time-resolved ellipsometry measurements, which may be related to our predicted sinking of the A point conduction band at x_{SMT}. However, no ultrafast inverse Peierls transition in Te has been experimentally reported to date.

Under an adiabatic approximation in which the electronic response time is much shorter than the characteristic phonon period, the time-dependent band structure as a function of $x(t)$ can be captured by static DFT calculations as a function of x [10]. Therefore, experimental verification of the light-induced structural changes calculated using TDDFT serves as indirect evidence of the predicted three-state switch between a WS, WM, and DM.

III. EXPERIMENTAL RESULTS

To quantitatively test our TDDFT predictions, we performed time-resolved optical second harmonic generation rotational anisotropy (SHG-RA) measurements [Fig. 3(e), inset] [13,38]. Since the leading order electric-dipole contribution to SHG directly couples to the inversion odd structural order parameter of Te [39], this technique is simultaneously sensitive to the metastable x coordinate and the A_1 phonon properties under identical experimental conditions. Static SHG-RA patterns were measured using 1.5 eV incident probe light on Te single crystals polished with the c axis parallel to the surface plane. By acquiring patterns in both parallel (S_{in}-S_{out}) and crossed (S_{in}-P_{out}) polarization channels, we verified that the entire signal is attributable to a bulk electric-dipole SHG susceptibility tensor respecting D_3 symmetry [13].

Figures 3(a)–3(d) show instantaneous SHG-RA patterns in the S_{in}-S_{out} channel measured immediately after exciting with a 1 eV pump pulse of 100 fs duration—matching our TDDFT parameters—for different absorbed fluence levels. Note that the absorbed fluence is lower than the applied fluence by a factor of $1 - R$, where R is the reflectance at 1 eV. The instantaneous patterns exhibit a uniform (independent of scattering plane angle ϕ) decrease in intensity relative to the equilibrium pattern, indicating that all electric-dipole susceptibility tensor elements are suppressed by the same scale factor [13]. Since each tensor element is proportional to the structural order parameter, this confirms that pump excitation acts simply to reduce the structural order parameter and does not induce any symmetry breaking. The patterns subsequently undergo uniform oscillations about the reduced intensity value, consistent with a totally symmetric A_1 breathing mode [13]. By tracking the time dependence of the SHG intensity at $\phi = 0°$ [Figs. 3(e)–3(h)], we clearly resolve an intensity drop upon pump excitation on the timescale of a half cycle of the A_1 mode, followed by A_1 mode oscillations. While the oscillations are damped out after approximately 2 ps, the intensity offset persists out to at least 10 ps [13].

To directly compare the predicted and measured structural dynamics, we fit both $x(t)$ obtained from our TDDFT simulations [Fig. 2(a)] and the differential SHG
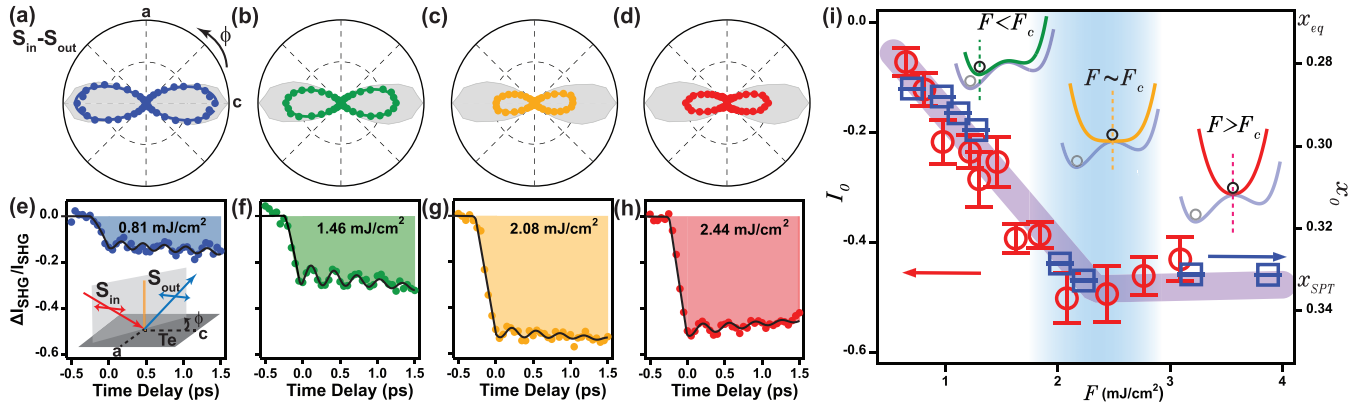
FIG. 3. Fluence dependence of the metastable structure. (a)–(d) Instantaneous SHG-RA patterns measured at $t = 50$ fs for different absorbed pump fluence values. The static ($t < 0$) pattern is overlaid and shaded gray. (e)–(h) Normalized differential SHG intensity transients acquired at the angle of maximum intensity ($\phi = 0°$) in the S_{in}-S_{out} pattern for each fluence. Solid lines are fits to an exponential decaying oscillation plus a constant offset (see text). A weak linear background was introduced in some traces to account for laser power drift. The inset in (e) shows a schematic of the SHG-RA setup. The scattering plane angle ϕ is measured with respect to the crystallographic c axis. Red, blue, and orange lines represent the incident, reflected SHG, and pump beams, respectively. (i) Pump fluence dependence of the measured SHG offset term (red circles) and TDDFT calculated metastable x position (blue squares). The blue shaded bar indicates the critical fluence regime. Insets show schematics of the transient potential energy surface in the low-, critical-, and high-fluence regimes, illustrating the shift in the metastable x position from equilibrium (gray curves).

transients [Figs. 3(e)–3(h)] for $t > 0$ to the function $Ae^{-t/\tau} \cos(2\pi\nu t + \varphi) + B$. This expression includes the phonon amplitude A, damping time τ, phase φ, frequency ν, and a constant offset of the x coordinate ($B = x_0$) or SHG intensity ($B = I_0$). Focusing first on the offset term, we plot in Fig. 3(i) the fitted values of x_0 for multiple fluences. In the weak-excitation regime, x_0 increases monotonically with fluence, indicating a shift of the potential energy minimum towards the centrosymmetric position. At a critical fluence near 2 mJ/cm², the Peierls nondistorted structure is reached, and the potential energy surface becomes parabolic with a minimum at x_{SPT}. Further increasing the fluence alters the curvature of the parabola but leaves x_0 fixed at x_{SPT}. The fitted values of I_0 acquired over a similar fluence range are overlaid [Fig. 3(i)], which not only obey a trend qualitatively similar to x_0 but also show a quantitatively matching critical fluence value. These results suggest an experimental realization of a light-induced inverse Peierls transition. We note that the comparison is not exact because the SHG intensity saturates to a nonzero value. Such residual signals are commonly observed across photoinduced phase transitions [11,28,40,41]. They may be attributed to incomplete order parameter suppression within the probed volume due to quench-induced spatial domains and defects [42], penetration depth mismatch between pump and probe beams [13,40], spatial nonuniformity of the pump intensity [11], or higher-multipole SHG radiation processes, all of which are not accounted for by our TDDFT simulations.

The dynamics of the coherent A_1 phonon can serve as an additional diagnostic, as schematically depicted in Figs. 4(a)–4(c). For an ultrafast inverse Peierls distortion, one expects that as the fluence increases towards F_c, the potential energy minimum should be displaced further away from x_{eq}, and its curvature should decrease as the landscape evolves from being locally parabolic to locally quartic. As illustrated in Fig.4(a), the former causes the phonon amplitude to increase, while

the latter causes the phonon frequency to decrease. At F_c, the displacement reaches its maximum value of $x_{SPT} - x_{eq}$, so the phonon amplitude saturates [Fig. 4(b)]. On the other hand, the landscape becomes parabolic again above F_c, so the curvature starts to increase with fluence, corresponding to an increasing phonon frequency [Fig. 4(c)].
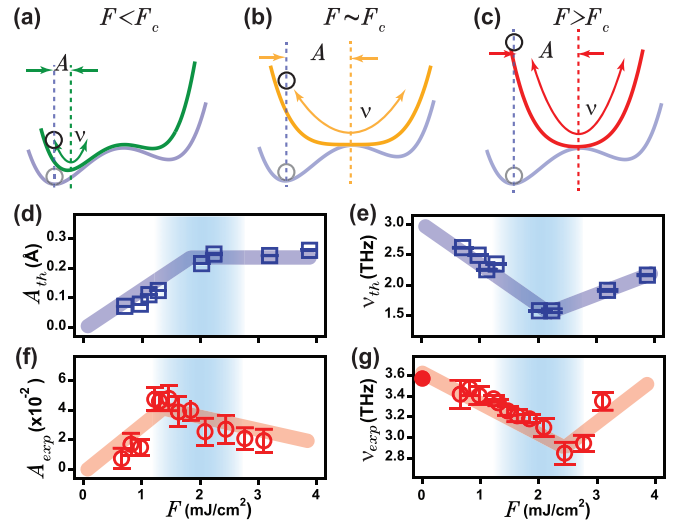

FIG. 4. Fluence dependence of the coherent A_1 phonon dynamics. (a)–(c) Schematics of the metastable potential energy surface at select fluences. The separation between the vertical dashed lines sets the phonon amplitude A, and the curvature of the potential minimum sets the phonon frequency ν. (d) Simulated pump fluence dependence of the phonon amplitude and (e) frequency obtained from TDDFT [13]. (f) Experimentally measured fluence dependence of the phonon amplitude and (g) frequency obtained by fitting the SHG transients in Figs. 3(e)–3(h). The solid circle at $F = 0$ in (g) is measured with Raman scattering [13]. The shaded blue bars mark the critical regime.

Figures 4(d) and 4(e) show the fluence dependence of A_{th} and ν_{th} extracted from fits to the TDDFT simulations. Subscripts on the phonon parameters denote theoretical (th) or experimental (exp) values. The anticipated saturation behavior of A_{th} and softening and rehardening behavior of ν_{th} are clearly borne out. Turning to the transient SHG data, we resolve coherent phonon oscillations both below and above F_c [Figs. 3(e)–3(h)], indicating that Te remains crystalline over our measured fluence range [13]. As shown in Fig. 4(f), A_{exp} increases with fluence in the weak-excitation regime and then abruptly changes slope just below F_c, reminiscent of A_{th}. However, unlike A_{th}, A_{exp} does not saturate above F_c but instead exhibits a slightly downward slope. Although the origin of this discrepancy with TDDFT is unclear, a similar downward trend has been reported above other ultrafast SPTs [11] and may be related to cumulative heating, electronic diffusion, and changes in the Raman scattering cross section of probe photons, which are not accounted for in TDDFT. Figure 4(g) shows that ν_{exp} decreases with fluence from its 3.6 THz equilibrium value in the weak-excitation regime. This is quantitatively consistent with previous studies on Te [25,31] and indicates that TDDFT slightly underestimates the frequency. Above approximately 2 mJ/cm^2, there is an abrupt change in slope from negative to positive, closely following the behavior of ν_{th}.

IV. DISCUSSION

The consistency between our TDDFT simulations and time-resolved SHG experiments across multiple observables establishes that light can be used to tune elemental Te across an inverse Peierls transition. Our TDDFT results show that this SPT should be accompanied by an ultrafast switching from WS to metastable WM and DM states. Although structural probes, while indirect, have commonly been used to infer the changes in electronic structure [10,11], the topological band structure change may be directly verifiable in the future using high-resolution extreme ultraviolet time-, spin-, and angle-resolved photoemission spectroscopy. Moreover, our work showcases the effectiveness of TDDFT in predicting impulsively driven out-of-equilibrium SPTs. More generally, note that this inverse Peierls distortion may also be induced entirely through lattice degrees of freedom via ionic Raman scattering [13,43]. Therefore, our results suggest that three-dimensional Peierls systems are a vast and fertile playground for exploring the interplay of ultrafast insulator-to-metal transitions and ultrafast band topology control, two hitherto disparate areas of research. As embodied by Te, this research possibly paves the way towards multistate-switchable and multifunctional ultrafast Weyl devices.

[1] B. Yan and C. Felser, Annu. Rev. Condens. Matter Phys. **8**, 337 (2017).

[2] H. Hübener, M. A. Sentef, U. De Giovannini, A. F. Kemper, and A. Rubio, Nat. Commun. **8**, 13940 (2017).

[3] C.-K. Chan, Y.-T. Oh, J. H. Han, and P. A. Lee, Phys. Rev. B **94**, 121106(R) (2016).

[4] Z. Yan and Z. Wang, Phys. Rev. Lett. **117**, 087402 (2016).

[5] G. E. Topp, N. Tancogne-Dejean, A. F. Kemper, A. Rubio, and M. A. Sentef, Nat. Commun. **9**, 4452 (2018).

[6] M.-X. Guan, E. Wang, P.-W. You, J.-T. Sun, and S. Meng, Nat. Commun. **12**, 1885 (2021).

[7] S. Ebihara, K. Fukushima, and T. Oka, Phys. Rev. B **93**, 155107 (2016).

[8] C. Vaswani, L.-L. Wang, D. H. Mudiyanselage, Q. Li, P. M. Lozano, G. D. Gu, D. Cheng, B. Song, L. Luo, R. H. J. Kim, C. Huang, Z. Liu, M. Mootz, I. E. Perakis, Y. Yao, K. M. Ho, and J. Wang, Phys. Rev. X **10**, 021013 (2020).

[9] L. Luo, D. Cheng, B. Song, L.-L. Wang, C. Vaswani, P. M. Lozano, G. Gu, C. Huang, R. H. J. Kim, Z. Liu, J.-M. Park, Y. Yao, K. Ho, I. E. Perakis, Q. Li, and J. Wang, Nat. Mater. **20**, 329 (2021).

[10] E. J. Sie et al., Nature (London) **565**, 61 (2019).

[11] M. Y. Zhang, Z. X. Wang, Y. N. Li, L. Y. Shi, D. Wu, T. Lin, S. J. Zhang, Y. Q. Liu, Q. M. Liu, J. Wang, T. Dong, and N. L. Wang, Phys. Rev. X **9**, 021036 (2019).

[12] P. Tangney and S. Fahy, Phys. Rev. B **65**, 054302 (2002).

[13] See Supplemental Material at http://link.aps.org/supplemental/10.1103/PhysRevB.106.205118 for extensive simulation and experimental details. See also Refs. [44–76] therein.

[14] G. Chang, B. J. Wieder, F. Schindler, D. S. Sanchez, I. Belopolski, S.-M. Huang, B. Singh, D. Wu, T.-R. Chang, T. Neupert, S.-Y. Xu, H. Lin, and M. Z. Hasan, Nat. Mater. **17**, 978 (2018).

[15] K. Nakayama, M. Kuno, K. Yamauchi, S. Souma, K. Sugawara, T. Oguchi, T. Sato, and T. Takahashi, Phys. Rev. B **95**, 125204 (2017).

[16] M. Sakano et al., Phys. Rev. Lett. **124**, 136404 (2020).

[17] G. Gatti et al., Phys. Rev. Lett. **125**, 216402 (2020).

[18] N. Zhang, G. Zhao, L. Li, P. Wang, L. Xie, B. Cheng, H. Li, Z. Lin, C. Xi, J. Ke, M. Yang, J. He, Z. Sun, Z. Wang, Z. Zhang, and C. Zeng, Proc. Natl. Acad. Sci. USA **117**, 11337 (2020).

[19] M. Hirayama, R. Okugawa, S. Ishibashi, S. Murakami, and T. Miyake, Phys. Rev. Lett. **114**, 206401 (2015).

[20] L. A. Agapito, N. Kioussis, W. A. Goddard, and N. P. Ong, Phys. Rev. Lett. **110**, 176401 (2013).

[21] X.-X. Xue, Y.-X. Feng, L. Liao, Q.-J. Chen, D. Wang, L.-M. Tang, and K. Chen, J. Phys.: Condens. Matter **30**, 125001 (2018).

[22] D. Rodriguez, A. A. Tsirlin, T. Biesner, T. Ueno, T. Takahashi, K. Kobayashi, M. Dressel, and E. Uykur, Phys. Rev. Lett. **124**, 136402 (2020).

[23] T. Ideue, M. Hirayama, H. Taiko, T. Takahashi, T. Murase, T. Miyake, S. Murakami, T. Sasagawa, and Y. Iwasa, Proc. Natl. Acad. Sci. USA **116**, 25530 (2019).

[24] H. J. Zeiger, J. Vidal, T. K. Cheng, E. P. Ippen, G. Dresselhaus, and M. S. Dresselhaus, Phys. Rev. B **45**, 768 (1992).

[25] S. W. Teitelbaum, T. Shin, J. W. Wolfson, Y.-H. Cheng, I. J. Porter, M. Kandyla, and K. A. Nelson, Phys. Rev. X **8**, 031081 (2018).

[26] S. Wall, Jr., D. Wegkamp, L. Foglia, K. Appavoo, J. Nag, R. F. Haglund, J. Stähler, and M. Wolf, Nat. Commun. **3**, 721 (2012).

[27] S. Wall, B. Krenzer, S. Wippermann, S. Sanna, F. Klasing, A. Hanisch-Blicharski, M. Kammler, W. G. Schmidt, and M. Horn-von Hoegen, Phys. Rev. Lett. **109**, 186101 (2012).

[28] T. Huber, S. O. Mariager, A. Ferrer, H. Schäfer, J. A. Johnson, S. Grübel, A. Lübcke, L. Huber, T. Kubacka, C. Dornes, C. Laulhe, S. Ravy, G. Ingold, P. Beaud, J. Demsar, and S. L. Johnson, Phys. Rev. Lett. **113**, 026401 (2014).

[29] P. Beaud *et al.*, Nat. Mater. **13**, 923 (2014).

[30] S. L. Johnson, E. Vorobeva, P. Beaud, C. J. Milne, and G. Ingold, Phys. Rev. Lett. **103**, 205501 (2009).

[31] T. Dekorsy, H. Auer, C. Waschke, H. J. Bakker, H. G. Roskos, H. Kurz, V. Wagner, and P. Grosse, Phys. Rev. Lett. **74**, 738 (1995).

[32] S. Hunsche, K. Wienecke, T. Dekorsy, and H. Kurz, Phys. Rev. Lett. **75**, 1815 (1995).

[33] N. Kamaraju, S. Kumar, M. Anija, and A. K. Sood, Phys. Rev. B **82**, 195202 (2010).

[34] Y.-H. Cheng, S. W. Teitelbaum, F. Y. Gao, and K. A. Nelson, Phys. Rev. B **98**, 134112 (2018).

[35] V. Iyer, M. Segovia, Y. Wang, W. Wu, P. Ye, and X. Xu, Phys. Rev. B **100**, 075436 (2019).

[36] G. Jnawali, Y. Xiang, S. M. Linser, I. A. Shojaei, R. Wang, G. Qiu, C. Lian, B. M. Wong, W. Wu, P. D. Ye, Y. Leng, H. E. Jackson, and L. M. Smith, Nat. Commun. **11**, 3991 (2020).

[37] A. M.-T. Kim, C. A. D. Roeser, and E. Mazur, Phys. Rev. B **68**, 012301 (2003).

[38] D. H. Torchinsky, H. Chu, T. Qi, G. Cao, and D. Hsieh, Rev. Sci. Instrum. **85**, 083102 (2014).

[39] M. Cheng, S. Wu, Z.-Z. Zhu, and G.-Y. Guo, Phys. Rev. B **100**, 035202 (2019).

[40] A. Kogar *et al.*, Nat. Phys. **16**, 159 (2020).

[41] A. D. Caviglia *et al.*, Phys. Rev. B **88**, 220401(R) (2013).

[42] R. Yusupov, T. Mertelj, V. V. Kabanov, S. Brazovskii, P. Kusar, J.-H. Chu, I. R. Fisher, and D. Mihailovic, Nat. Phys. **6**, 681 (2010).

[43] M. Först, R. Mankowsky, and A. Cavalleri, Acc. Chem. Res. **48**, 380 (2015).

[44] P. Giannozzi *et al.*, J. Phys.: Condens. Matter **21**, 395502 (2009).

[45] P. Giannozzi, Jr., *et al.*, J. Phys.: Condens. Matter **29**, 465901 (2017).

[46] P. Tangney and S. Fahy, Phys. Rev. Lett. **82**, 4340 (1999).

[47] C. Lian, S.-Q. Hu, M.-X. Guan, and S. Meng, J. Chem. Phys. **149**, 154104 (2018).

[48] C. Lian, M. Guan, S. Hu, J. Zhang, and S. Meng, Adv. Theory Simul. **1**, 1800055 (2018).

[49] C. Lian, S.-J. Zhang, S.-Q. Hu, M.-X. Guan, and S. Meng, Nat. Commun. **11**, 1 (2020).

[50] E. Runge and E. K. U. Gross, Phys. Rev. Lett. **52**, 997 (1984).

[51] G. F. Bertsch, J.-I. Iwata, A. Rubio, and K. Yabana, Phys. Rev. B **62**, 7998 (2000).

[52] Z. Wang, S.-S. Li, and L.-W. Wang, Phys. Rev. Lett. **114**, 063004 (2015).

[53] J. P. Perdew, K. Burke, and M. Ernzerhof, Phys. Rev. Lett. **77**, 3865 (1996).

[54] M. van Setten, M. Giantomassi, E. Bousquet, M. Verstraete, D. Hamann, X. Gonze, and G.-M. Rignanese, Comput. Phys. Commun. **226**, 39 (2018).

[55] S. Tutihasi, G. G. Roberts, R. C. Keezer, and R. E. Drews, Phys. Rev. **177**, 1143 (1969).

[56] S. Lin, W. Li, Z. Chen, J. Shen, B. Ge, and Y. Pei, Nat. Commun. **7**, 10287 (2016).

[57] C. Hejny and M. I. McMahon, Phys. Rev. Lett. **91**, 215502 (2003).

[58] C. Hejny and M. I. McMahon, Phys. Rev. B **70**, 184109 (2004).

[59] C. Hejny, S. Falconi, L. F. Lundegaard, and M. I. McMahon, Phys. Rev. B **74**, 174119 (2006).

[60] V. T. Deshpande and R. Pawar, Physica (Amsterdam) **31**, 671 (1965).

[61] S. I. Ashitkov, M. B. Agranat, P. S. Kondratenko, S. I. Anisimov, V. E. Fortov, V. V. Temnov, K. Sokolowski-Tinten, B. Rethfeld, P. Zhou, and D. von der Linde, JETP Lett. **76**, 461 (2002).

[62] M. H. Brodsky, R. J. Gambino, J. E. Smith, Jr., and Y. Yacoby, Phys. Status Solidi B **52**, 609 (1972).

[63] S. Hunsche, K. Wienecke, and H. Kurz, Appl. Phys. A **62**, 499 (1996).

[64] S. I. Kudryashov, M. Kandyla, C. A. D. Roeser, and E. Mazur, Phys. Rev. B **75**, 085207 (2007).

[65] O. V. Misochko and M. V. Lebedev, Phys. Rev. B **94**, 184307 (2016).

[66] M. Först, C. Manzoni, S. Kaiser, Y. Tomioka, Y. Tokura, R. Merlin, and A. Cavalleri, Nat. Phys. **7**, 854 (2011).

[67] D. M. Juraschek, M. Fechner, and N. A. Spaldin, Phys. Rev. Lett. **118**, 054101 (2017).

[68] M. Rini, R. Tobey, N. Dean, J. Itatani, Y. Tomioka, Y. Tokura, R. W. Schoenlein, and A. Cavalleri, Nature (London) **449**, 72 (2007).

[69] D. Fausti, R. I. Tobey, N. Dean, S. Kaiser, A. Dienst, M. C. Hoffmann, S. Pyon, T. Takayama, H. Takagi, and A. Cavalleri, Science **331**, 189 (2011).

[70] R. Mankowsky, A. Subedi, M. Först, S. O. Mariager, M. Chollet, H. T. Lemke, J. S. Robinson, J. M. Glownia, M. P. Minitti, A. Frano, M. Fechner, N. A. Spaldin, T. Loew, B. Keimer, A. Georges, and A. Cavalleri, Nature (London) **516**, 71 (2014).

[71] M. Mitrano, A. Cantaluppi, D. Nicoletti, S. Kaiser, A. Perucchi, S. Lupi, P. Di Pietro, D. Pontiroli, M. Riccò, S. R. Clark, D. Jaksch, and A. Cavalleri, Nature (London) **530**, 461 (2016).

[72] M. Gu and J. M. Rondinelli, Phys. Rev. B **98**, 024102 (2018).

[73] T. F. Nova, A. Cartella, A. Cantaluppi, M. Först, D. Bossini, R. V. Mikhaylovskiy, A. V. Kimel, R. Merlin, and A. Cavalleri, Nat. Phys. **13**, 132 (2017).

[74] T. F. Nova, A. S. Disa, M. Fechner, and A. Cavalleri, Science **364**, 1075 (2019).

[75] D. Afanasiev, J. R. Hortensius, B. A. Ivanov, A. Sasani, E. Bousquet, Y. M. Blanter, R. V. Mikhaylovskiy, A. V. Kimel, and A. D. Caviglia, Nat. Mater. **20**, 607 (2021).

[76] A. von Hoegen, R. Mankowsky, M. Fechner, M. Först, and A. Cavalleri, Nature (London) **555**, 79 (2018).